ACS APPLIED MATERIALS & INTERFACES

www.acsami.org

Research Article

Crystal Violet-Sensitized Direct Z-Scheme Heterojunction Coupled with a G-Wire Superstructure for Photoelectrochemical Sensing of Uracil-DNA Glycosylase

Xing Yue Zhang, Lei Han, Ling Dan Yu, Xiao Hu Wang, Yu Ling, Nian Bing Li,* and Hong Qun Luo*

Cite This: *ACS Appl. Mater. Interfaces* 2021, 13, 15881−15889

Read Online

ACCESS | Metrics & More | Article Recommendations | Supporting Information

ABSTRACT: Dye sensitization achieving photoelectrochemical (PEC) signal amplification for ultrasensitive bioanalysis has undergone a major breakthrough. In this proposal, an innovative PEC sensing platform is developed by combining Z-scheme WO_3@SnS_2 photoactive materials and a G-wire superstructure as well as a dye sensitization enhancement strategy. The newly synthesized WO_3@SnS_2 heterojunction with outstanding PEC performance is employed as a photoelectrode matrix. Due to the formation of the Z-scheme heterojunction between WO_3 and SnS_2, the migration dynamics of the photogenerated carrier is evidently augmented. To improve sensitivity, the target excision-driven dual-cycle signal amplification strategy is introduced to output exponential c-myc fragments. Crystal violet is then conjugated into the G-quadruplex to amplify the PEC signal, where crystal violet generates excited electrons by capturing visible light and rapidly injects electrons into the conduction band of SnS_2, suppressing the recombination of the photo-induced carrier. Moreover, the G-wire superstructure acts as a universal amplification pathway, ensuring adequate crystal violet loads. Specifically, the biosensor for uracil-DNA glycosylase quantification displays a wide detection range (0.0005−1.0 U/mL) and a lower detection limit (0.00025 U/mL). Furthermore, the Z-scheme electron migration mechanism and the crystal violet sensitization effect are discussed in detail. The construction of the PEC sensor provides a new consideration for signal amplification and material design.

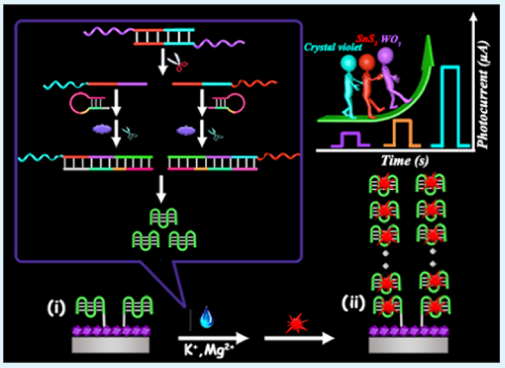

KEYWORDS: *photoelectrochemical biosensor, Z-scheme heterojunction, dye sensitization, crystal violet, G-wire superstructure*

1. INTRODUCTION

Uracil-DNA glycosylase (UDG), a highly conserved base excision repair enzyme, is responsible for guaranteeing genetic integrity.[1] It can specifically recognize and liberate uracil base from DNA by catalyzing the cleavage of the *N*-glycosidic bond that connects the uracil base to deoxyribose.[2] In this regard, abnormal UDG activity can lead to dysregulation of uracil excision and ultimately cause various diseases, including neurodegeneration, human immunodeficiency, and even cancers.[3−5] Hence, accurate assessment of UDG activity is of great significance for both clinical diagnosis and biomedicine. Photoelectrochemical (PEC) biosensing possesses some potential advantages, such as inherent high sensitivity caused by the separation of the detection signal and the excitation light source,[6] miniaturization of instruments, and low cost. Generally, to implement a sensitive PEC sensing system, two critical parts are indispensable: a photoactive material and a signal amplification unit.

Specifically, the preparation of highly active photoelectrochemical materials is considered as one of the key steps in the design of high-performance PEC sensors. Thereinto, the nature-inspired Z-scheme photoactive material system can dramatically inhibit the electron−hole recombination and improve detection sensitivity for PEC sensing due to the high charge separation quantum efficiency.[7,8] However, most Z-scheme systems are conventional all-solid-state Z-schemes,[9−11] which consist of a kind of noble-metal nanoparticle and two different semiconductors as the shuttle mediator. These shuttle mediators will increase the cost or hinder light absorption by photoactive materials.[12,13] For direct Z-scheme photoactive materials, the close interfacial contact and strong electronic interaction between two different semiconductors can lead to the formation of an internal electric field, guaranteeing efficacious charge separation and transfer without any shuttle mediators.[14−16] Among diverse photoactive materials, tungsten trioxide (WO_3) displays a comprehensive application foreground in the photocatalytic field in terms of its intrinsic optical properties and nontoxicity.[17,18] Moreover, the WO_3

Received: January 23, 2021
Accepted: March 18, 2021
Published: March 28, 2021

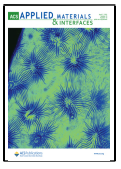

https://doi.org/10.1021/acsami.1c01525
ACS Appl. Mater. Interfaces 2021, 13, 15881−15889

Scheme 1. Schematic Illustration of (a) Synthesis Process for the WO_3@SnS_2 Hierarchical Nanostructure, (b) PEC Sensing Platform Construction and UDG Excision Assay, and (c) PEC Response and Signal Enhancement Mechanism

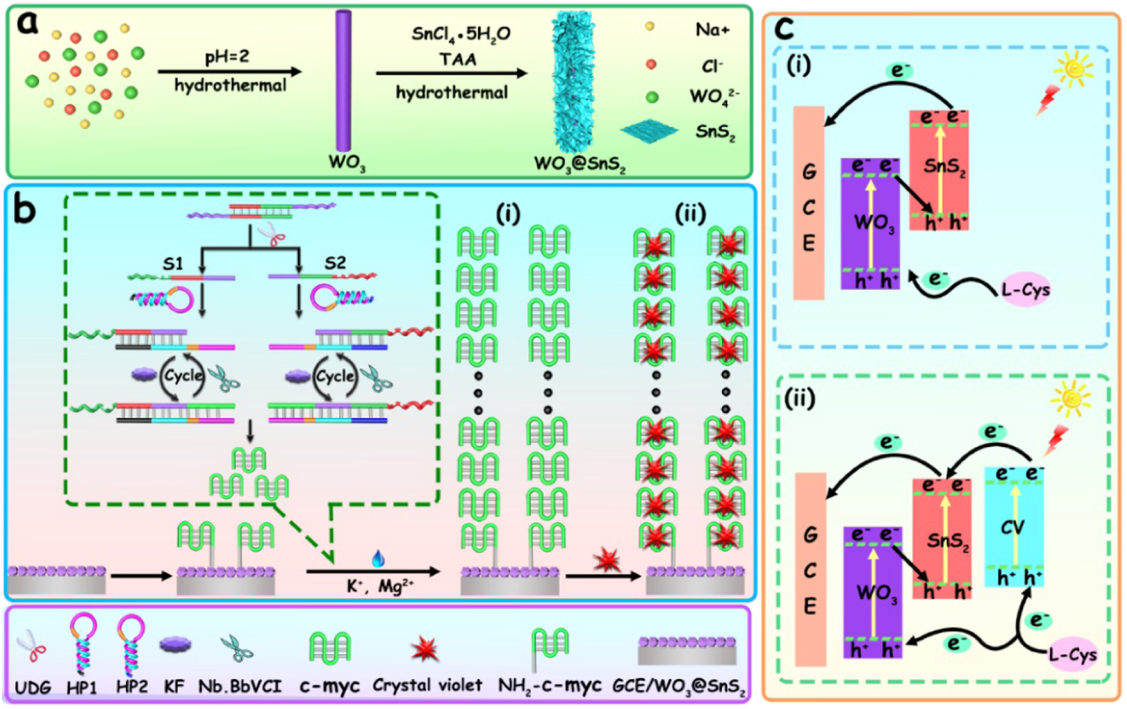

with a rodlike morphology is favorable for electron migration, and the rodlike structure with a large surface area can be decorated with other functional materials or auxiliary catalysts to promote the transport of charge carrier. SnS_2, a metal sulfide semiconductor material, possesses remarkable visible light response activity, a unique electronic structure, and super-electronic conductivity.[19,20] Furthermore, the two-dimensional (2D) conformation of nanosheets is beneficial to decrease the diffusion distance of photogenerated carriers and improve the separation efficiency of charge carriers. Despite these advantages, the photoelectric conversion efficiency of SnS_2 is not ideal due to the slow separation and migration kinetics of photogenerated carriers. It is necessary to solve this problem, and rational tailoring and design of the contact interface in the hybrid system will provide the driving force for the separation of holes and electrons. To this end, by integrating WO_3 and SnS_2 into a hierarchical nanostructure to construct a Z-scheme heterostructure, the WO_3@SnS_2 heterojunctions are endowed with elegant merits, including an extended light absorption range to longer wavelength and ameliorated charge-transfer efficiency, which is further converted into improved performance in PEC biosensor applications.

Aside from the attractive photoactive materials, the signal amplification may affect detection sensitivity. Various effective signal amplification methods have been developed to meet the requirement of high-sensitivity detection, for example, enzyme-catalyzed in situ precipitation,[21−23] in situ generation of electron donors,[24−26] dye sensitization,[27,28] in situ generation of photoactive materials,[29,30] and so forth. On account of the merits of dyes including a wide absorption range, high light absorption efficiency, and diverse electronic structure, dye sensitization has become a striking signal amplification strategy. As a triphenylmethane dye, crystal violet (CV) has been gaining considerable momentum in fluorescent biosensors due to its conjugated π electronic structure, fast electron injection dynamics, excellent visible light absorption properties, and low cost.[31−33] Moreover, it shows superior interactions with the negatively charged phosphate backbone and can stack onto the G-quadruplex through three phenyl rings.[34] Notably, c-myc, a telomeric oligonucleotide, can form a G-quadruplex with the aid of K^+, and further stack to develop a G-wire superstructure with abundant repeated G-quadruplex units in the presence of Mg^{2+}.[35] Strand displacement amplification (SDA) is a simple and efficient signal amplification strategy that can produce a large number of identical oligonucleotide fragments in a short time by target molecules or initiators.[36,37] Hence, a PEC biosensing platform for UDG detection was constructed, in which signal amplification was achieved by UDG-assisted excision-driven SDA by indirectly growing a G-wire as a carrier for dye sensitizer immobilization.

Herein, we elaborately constructed a "signal-on" PEC biosensing platform for ultrasensitive UDG detection based on a Z-scheme WO_3@SnS_2 hierarchical nanostructure coupled with the unique superstructure of a G-wire and a crystal violet enhancement strategy. Furthermore, the purpose of this work is not only to explore a novel sensitizer but also to study the charge-transfer mechanism of a photoactive material and the sensitization enhancement mechanism. As depicted in Scheme 1b, the WO_3@SnS_2 hierarchical nanostructure as a photoactive material was applied for the photoelectrode matrix. Amino-functionalized c-myc sequences as substrates for growing a G-wire were covalently attached to the surface of a modified electrode. At the same time, UDG excision-driven enzyme-assisted dual-cycle signal amplification was performed (see the Supporting Information for the experimental process and the polyacrylamide gel electrophoresis (PAGE) characterization; Figure S1). In this process, dsDNA and two thermodynamically stable hairpins (HP1 and HP2; Table S1) were exquisitely and reasonably designed, in which dsDNA and hairpins do not

https://doi.org/10.1021/acsami.1c01525
ACS Appl. Mater. Interfaces 2021, 13, 15881−15889

react with each other without UDG. The introduction of UDG can remove uracil from U−A pairs in the dsDNA, resulting in attenuation in the stability of dsDNA and dissociation to form two single strands (S1 and S2). The released single-strand DNA functions as a trigger to open hairpins separately, and initiate strand displacement amplification, producing plenty of c-myc fragments. Subsequently, the c-myc regions stacked to form a long filamentous G-wire structure in the presence of metal ions, which was immobilized onto the substrate. Ultimately, CV, serving as a signal enhancer, is stably conjugated into the face of the G-quadruplex in the G-wires via $\pi-\pi$ stacking and electrostatic interactions to magnify the PEC response, thereby achieving a sensitive UDG activity assay. This work is expected to inspire the design of more advanced PEC biosensors based on the crystal violet enhancement strategy and exploration of more signal intensifiers for the construction of PEC sensing systems.

2. RESULTS AND DISCUSSION

2.1. Morphological and Structural Characterization of Photoactive Materials. Scheme 1a depicts the construction process of the WO_3@SnS_2 hierarchical nanostructure based on a two-step hydrothermal strategy (see the Supporting Information for the synthetic method). The morphologies of the as-prepared WO_3, SnS_2, and WO_3@SnS_2 hierarchical nanostructures were investigated by field emission scanning electron microscopy (FESEM). As shown in Figure 1a, the

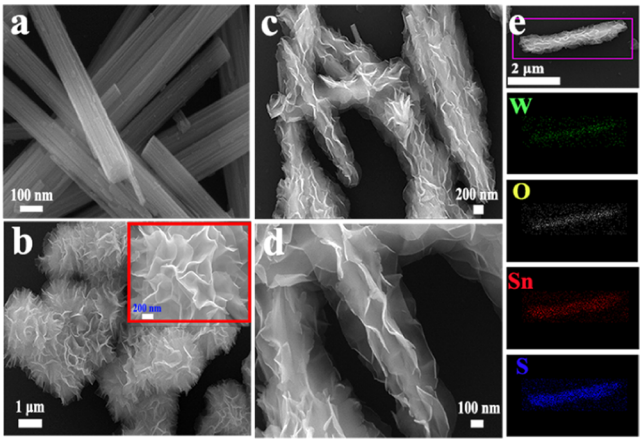

Figure 1. Scanning electron microscopy (SEM) image of (a) WO_3, (b) SnS_2, and (c, d) WO_3@SnS_2 hierarchical nanostructures. (e) Elemental mapping images of W, O, Sn, and S in the WO_3@SnS_2 hierarchical nanostructure. The region shown in (b) framed with the red line shows the high-magnification image of SnS_2.

pure WO_3 presents a homogeneous rodlike structure with a diameter of about 150 nm. The pure SnS_2 shows a marigold flower structure (Figure 1b), and the high-magnification image (the area shown in Figure 1b bound by the red line) shows that the SnS_2 nanoflower consists of a large number of nanosheets. Figure 1c displays the morphology of the as-prepared WO_3@SnS_2 hierarchical nanostructure, in which the WO_3 nanorods are uniformly encapsulated by the disorderly 2D SnS_2 nanosheets, and the high-magnification image (Figure 1d) suggests that the SnS_2 nanosheets are grown on the surface of the one-dimensional (1D) WO_3 nanorods. The grown nanosheets serve as efficacious light scattering units and trap light more fully. Furthermore, elemental mapping was used to study the elemental composition of as-prepared WO_3@SnS_2. It can be seen from Figure 1e that the elements of W, O, Sn, and S are evenly distributed on the surface of the WO_3@SnS_2 hierarchical nanostructure.

To gain a deeper understanding of the microstructure of WO_3@SnS_2, transmission electron microscopy (TEM) was subsequently performed. The TEM image of WO_3@SnS_2 in Figure 2a shows that ultrathin SnS_2 nanosheets are coated on

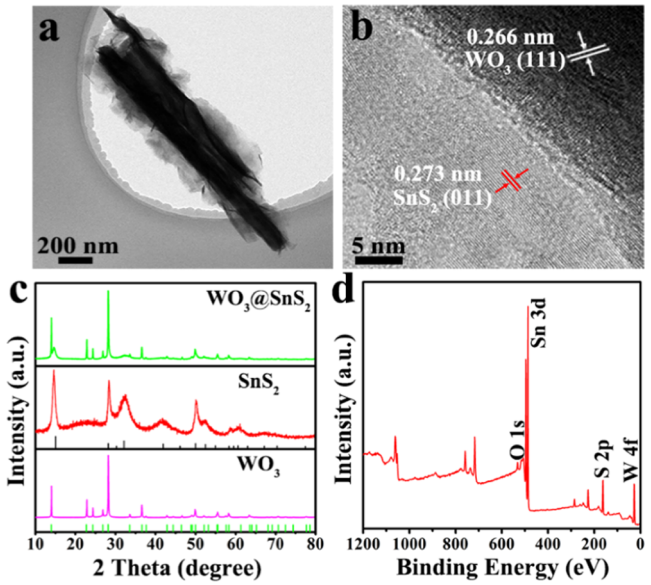

Figure 2. (a) TEM and (b) HRTEM images of the WO_3@SnS_2 hierarchical nanostructure. (c) X-ray diffraction (XRD) patterns of pure WO_3, SnS_2, and WO_3@SnS_2 hierarchical nanostructures. (d) X-ray photoelectron spectroscopy (XPS) survey of the WO_3@SnS_2 hierarchical nanostructure.

the surface of WO_3 nanorods. Also, the high-resolution TEM (HRTEM) demonstrates the existence of two different structural domains (Figure 2b). The lattice fringes with interplanar spacings of 0.266 and 0.273 nm agree well with the (111) plane of WO_3 and the (011) plane of SnS_2, respectively (Figure 2b). The obvious lattice interface between WO_3 and SnS_2 confirms the formation of the WO_3@SnS_2 heterojunction. It is worth noting that the formation of the three-dimensional (3D) hierarchical structure will shorten the charge-transfer distance and result in higher photoelectric conversion efficiency. In addition, the abundant interfaces between WO_3 and SnS_2 promote carrier separation, and the continuous interface delocalizes the charge carrier, which is more conducive to transport. These results suggest that the WO_3@SnS_2 hierarchical nanostructure possesses huge potential in PEC biosensing.

The X-ray diffraction (XRD) spectra were recorded to analyze the crystal structure of the samples (Figure 2c). All of the diffraction peaks of WO_3 agree well with those of the hexagonal WO_3 structure (JCPDS # 33-1387), and the sharp diffraction peaks confirm the high crystallinity of WO_3. Meanwhile, the major peaks can be indexed to the (100), (001), (110), (101), (200), (111), and (201) crystal planes. The diffraction peaks of SnS_2 reveal the phase structure, which can be attributed to the Berndtite-2T structure (JCPDS # 23-0677). In the XRD pattern of the WO_3@SnS_2 hierarchical nanostructure, all of the diffraction peaks can be indexed to the hexagonal WO_3 structure (JCPDS # 33-1387) and the

https://doi.org/10.1021/acsami.1c01525
ACS Appl. Mater. Interfaces 2021, 13, 15881−15889

Berndtite-2T structure of SnS_2 (JCPDS # 23-0677), showing the formation of the WO_3@SnS_2 nanostructure.

To further explore the electronic states and chemical interactions of the as-prepared samples, X-ray photoelectron spectroscopy (XPS) analysis was performed for the WO_3@SnS_2 hierarchical nanostructure, and the results were compared with single SnS_2 and WO_3. The survey XPS spectrum (Figure 2d) shows that the as-prepared WO_3@SnS_2 nanostructure is mainly composed of Sn, W, S, and O elements, which contain all of the elements in SnS_2 and WO_3, and no other impurities are found. Figure 3a–d displays the high-resolution spectra of

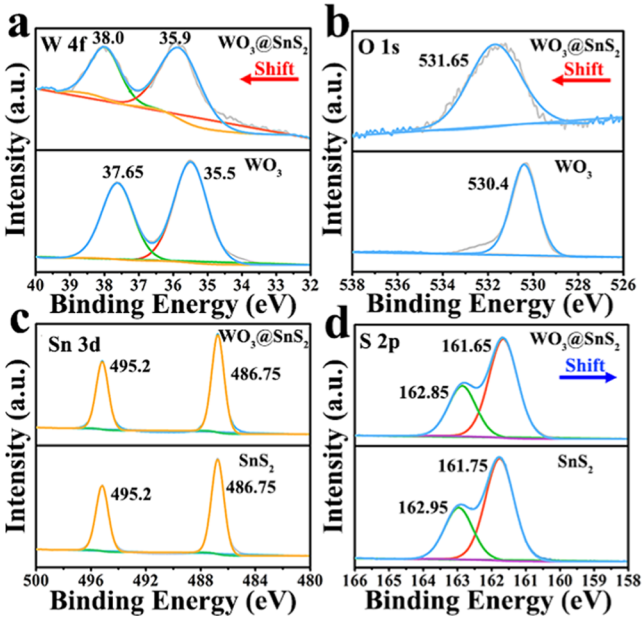

Figure 3. High-resolution XPS spectra of (a) W 4f, (b) O 1s, (c) Sn 3d, and (d) S 2p.

W 4f, O 1s, Sn 3d, and S 2p. The high resolution of the W 4f spectrum (Figure 3a) of the pristine WO_3 reveals that two peaks with binding energies of 35.5 and 37.65 eV are, respectively, assigned to W $4f_{7/2}$ and W $4f_{5/2}$ of W^{6+}.[17] The O 1s spectrum (Figure 3b) of pure WO_3 is centered at 530.4 eV, which is attributed to W–O.[38] As for the SnS_2 nanoflower, the Sn 3d includes two peaks at 486.75 eV (Sn $3d_{5/2}$) and 495.2 eV (Sn $3d_{3/2}$) (Figure 3c). Considering that the difference between the two strong Sn 3d peaks is about 8.4 eV, the Sn species exist in the form of Sn^{4+}.[39] As shown in Figure 3d, the peaks located at 161.75 and 162.95 eV in the high-resolution S 2p analysis of SnS_2 correspond to S $2p_{3/2}$ and S $2p_{1/2}$, which are in good agreement with S^{2-}.[20] When the SnS_2 nanosheets grew on the surface of WO_3 nanorods, the peaks of W 4f and O 1s in the WO_3@SnS_2 hierarchical nanostructure moved toward the positive binding energy compared with the peaks of single WO_3. This is due to the strong electronic coupling between WO_3 and SnS_2 caused by the change of the chemical environment. In contrast, the S 2p peaks of WO_3@SnS_2 present a distinct shift to lower binding energies relative to the peaks of SnS_2, which indicates an increase in the electron cloud density. Consequently, this change in the binding energy clearly indicates that electron transfer arises from WO_3 to SnS_2 on the WO_3@SnS_2 hierarchical nanostructure. Also, the movement of binding energy helps to establish an internal electric field at the interface between SnS_2 and WO_3, which will promote the separation and transfer of photogenerated carriers.

The interface charge separation efficiency was verified by the electrochemical impedance spectroscopy (EIS) measurement, which was performed in 0.1 M Na_2SO_4. As shown in Figure S2a, the charge-transfer resistance of WO_3@SnS_2 is smaller than that of SnS_2 and WO_3 both under dark and light conditions, indicating that the formation of the WO_3@SnS_2 heterojunction improves the conductivity and causes a rapid interfacial charge transfer. Moreover, the charge-transfer resistance of the samples under visible light irradiation is smaller than that of the samples under dark conditions, indicating that the separation efficiency of photogenerated electrons and holes can be effectively enhanced under visible light irradiation. On the other hand, compared with pristine WO_3 and SnS_2, a significantly enhanced photocurrent response produced on the WO_3@SnS_2 strongly demonstrates the promoted migration kinetics of the photogenerated carrier (Figure S2b). Moreover, the linear sweep voltammetry (LSV) curve of WO_3@SnS_2 under visible light irradiation displays an increase in photocurrent in the potential range of −0.2 to 0.5 V (Figure S2c). The increase of the photocurrent signal suggested high photon absorption, photoelectric conversion, and electron–hole separation efficiency at the WO_3@SnS_2 heterojunction interface. These electrochemical characterizations provide solid evidence for improving the separation and transfer dynamics of photogenerated carriers in the WO_3@SnS_2 hybrid material, which is ascribed to the unique interface interaction between WO_3 and SnS_2.

In addition, the optical absorption properties of as-prepared samples were studied by UV–vis diffuse reflectance spectroscopy (DRS), which are displayed in Figure 4a. It is clear that the pristine SnS_2 displays a wider absorption range compared with pristine WO_3. The absorption spectrum of SnS_2 covers visible light, but only less visible light can be absorbed by WO_3, indicating that SnS_2 is a potential visible-light-driven photoactive material. After the combination of WO_3 and SnS_2, the visible light absorption capability of the WO_3@SnS_2 nanostructure is significantly enhanced compared with WO_3. Furthermore, the WO_3@SnS_2 heterojunction exhibits high absorbed photon numbers (6.4×10^{14}) compared with pristine WO_3 (5.85×10^{14}) and SnS_2 (4.82×10^{14}). The broad absorption range and high absorbed photon numbers in the WO_3@SnS are attributed to the close interfacial contact and strong electronic interaction between WO_3 and SnS_2. Moreover, the energy gap of WO_3 and SnS_2 can be estimated using the following equation

$$\alpha h\nu = A(h\nu - E_g)^{n/2} \quad (1)$$

where α, h, ν, A, and E_g are the absorption coefficient, the Plank constant, the light frequency, the proportional constant, and the energy gap, respectively. Also, $n = 1$ for the direct band gap semiconductor and $n = 4$ for the indirect band gap semiconductor.[40] Figure 4b shows the curve of $(\alpha h\nu)^2$ vs $h\nu$ for SnS_2 and $(\alpha h\nu)^{1/2}$ against $h\nu$ for WO_3. Distinctly, the energy gaps of WO_3 and SnS_2 are calculated to be 2.85 and 1.98 eV, respectively. It is reported that the XPS valence spectra can be applied to study the energy gap from the valence band maximum (VBM) to the Fermi level (E_f) of semiconductor materials.[41,42] Apparently, from Figure 4c,d, the VBM positions of SnS_2 and WO_3 are found to be 1.83 and 2.63 eV below E_f. Figure 4e,f shows the Mott–Schottky plots of

https://doi.org/10.1021/acsami.1c01525
ACS Appl. Mater. Interfaces 2021, 13, 15881–15889

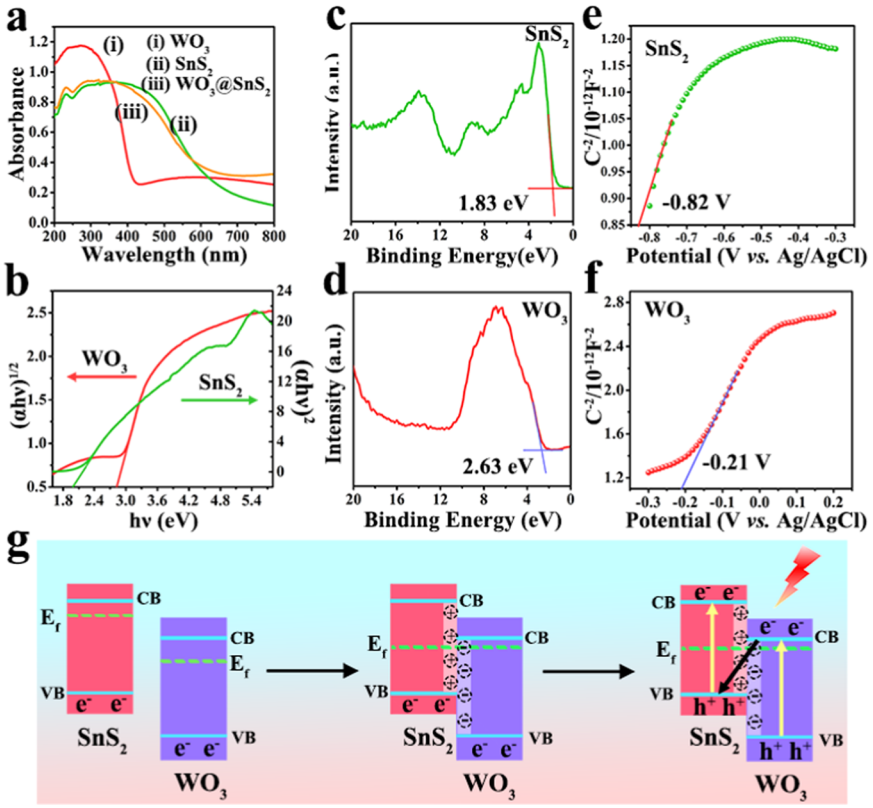

Figure 4. (a) UV−vis diffuse reflectance spectra (DRS) of pure WO_3, SnS_2, and WO_3@SnS_2 hierarchical nanostructures. (b) Plot of $(\alpha h\nu)^{1/2}$ vs $(h\nu)$ for WO_3 and $(\alpha h\nu)^2$ vs $(h\nu)$ for SnS_2. (c, d) Valance band XPS spectra of SnS_2 and WO_3, respectively. (e, f) Mott−Schottky plots of SnS_2 and WO_3, respectively. (g) Formation process of the internal electric field and the Z-scheme electron migration mechanism. The Mott−Schottky plot was measured in a 0.1 M Na_2SO_4 solution with an amplitude of 1 mV at a frequency of 1 kHz.

SnS_2 and WO_3 with positive slopes, further confirming the n-type semiconductor characteristics with electron conduction. The flat band potentials of WO_3 and SnS_2 are estimated to be −0.21 and −0.82 V vs Ag/AgCl through extrapolating the linear region of the Mott−Schottky plot to the *x*-axis, corresponding to −0.01 and −0.62 V vs the normal hydrogen electrode (NHE). As a result, the VBM values of SnS_2 and WO_3 are calculated to be 1.21 and 2.62 V (vs NHE), respectively. With the following equation

$$E_{CB} = E_{VB} - E_g \quad (2)$$

the values of E_{CB} are estimated to be −0.77 and −0.23 V (vs NHE) for SnS_2 and WO_3, respectively. Therefore, the electron migration between SnS_2 and WO_3 can be reasonably explained on the basis of the difference of the Fermi levels, which is inferred by XPS analysis. Figure 4g depicts an electron-transfer mechanism for the WO_3@SnS_2 hierarchical nanostructure. Specifically, since the Fermi level of SnS_2 is higher than that of WO_3, when the SnS_2 nanosheets come into contact with WO_3 nanorods, the electrons on the SnS_2 will migrate to WO_3 until their Fermi levels reach the same level, thus leaving a positive charge on the SnS_2 and a negative charge on the WO_3. Thus, an internal electric field is formed at their interface, and the direction of the internal electric field is from the SnS_2 to WO_3 surface. The formation of the internal electric field greatly facilitates the transfer of charge and improves the photoelectric conversion efficiency. On irradiation with photons, both the WO_3 and SnS_2 are excited to generate free electrons and holes; the electrons in the conduction band of WO_3 recombine with holes in the valence band of SnS_2, while the electrons in the conduction band of SnS_2 are injected to the electrode surface to produce anodic photocurrent, and the holes in the valence band of WO_3 are captured by hole-trapping reagents, facilitating the separation of holes and electrons. Therefore, a fascinating Z-scheme heterojunction was deftly constructed.

To further validate the formation of a direct Z-scheme heterojunction, a fluorescence test was carried out to survey the generation of hydroxyl radicals, which is one of the most common methods for detecting hydroxyl radicals.[43] Specifically, the photogenerated holes of a semiconductor with an oxidation potential greater than 2.4 V (vs NHE) can react with OH^-/H_2O, generating hydroxyl radicals upon light irradiation. It is well known that the nonfluorescent terephthalic acid (PTA) can react with hydroxyl radicals to yield highly fluorescent 2-hydroxyterephthalic acid. Obviously, WO_3@SnS_2 exhibits a prominent fluorescence peak at 425 nm compared with pristine SnS_2 and WO_3 under the same time light irradiation (Figure S3), indicating that many hydroxyl radicals are generated. This result shows that the photogenerated holes of WO_3@SnS_2 have sufficient oxidation potential to generate hydroxyl radicals. In fact, when a traditional type-II heterojunction is formed between WO_3 and SnS_2, the photogenerated holes will accumulate in the valence band of SnS_2. However, the valence band potential of SnS_2 is more negative than that of generated hydroxyl radicals, so it cannot interact with OH^-/H_2O to generate hydroxyl radicals, resulting in a low fluorescence. When the Z-scheme heterojunction is formed between WO_3 and SnS_2, the electron in the conduction band of WO_3 will transfer to the valence band of SnS_2 and the holes accumulated in the valence band of

https://doi.org/10.1021/acsami.1c01525
ACS Appl. Mater. Interfaces 2021, 13, 15881−15889

WO_3 with enough oxidation potential will interact with OH^-/H_2O to produce substantial hydroxyl radicals, obtaining high fluorescence. Hence, the result can further confirm the formation of the Z-scheme heterojunction between WO_3 and SnS_2. In addition, the pristine SnS_2 also produced weak fluorescence, which may be due to the indirect generation of hydroxyl radicals by superoxide anion radicals, which were generated by the photogenerated electrons on the conduction band of SnS_2.[43]

Furthermore, to study the sensitization enhancement mechanism, the energy band of crystal violet was obtained by optical measurement and organic-phase cyclic voltammetry. Figure S4a shows the cyclic voltammetry curve of crystal violet. Apparently, a reduction wave with an onset potential −0.699 V vs Ag/AgCl is acquired. According to the following equation

$$E_{CB} = -(E^{red}_{onset} - E^{+}_{Fc/Fc} + 4.8)\ \text{eV} \quad (3)$$

where E^{red}_{onset} and $E^{+}_{Fc/Fc}$ are the onset reduction potential and the reduction potential of Fc, respectively. The E_{CB} of the crystal violet is estimated to be −0.82 V (vs NHE). Moreover, the UV−visible absorption spectrum was recorded to evaluate the energy band. As depicted in Figure S4b, crystal violet has a strong absorption capacity in the range of visible light, and the absorption edge is located at 633 nm. Thus, the value of E_g for crystal violet is calculated to be 1.96 eV, and the E_{VB} is 1.14 V. The crystal violet with relatively negative conduction facilitates the injection of excited electrons.

2.2. Photoelectrochemical Response Mechanism. To perform ultrasensitive detection of UDG, we elaborately fabricated a label-free PEC sensing platform by combining a self-assembly G-wire nanostructure with a crystal violet enhancement strategy. As depicted in Scheme 1c, upon visible light irradiation, electrons in the valence band of WO_3 and SnS_2 are excited to the conduction band, in which the electron-transfer process and electron−hole pair recombination occur simultaneously. Due to the formation of direct Z-scheme electron transfer between WO_3 and SnS_2, the electron-transfer process is dominant, leading to a prominent photocurrent response. Subsequently, the G-wire nanostructure is formed based on the UDG excision driving strand displacement reaction, and a large amount of crystal violet is conjugated onto the G-wire nanostructure. Crystal violet with a wide absorption range from 400 to 650 nm exhibits an intense absorption at 590 nm ($6.65 \times 10^4\ M^{-1}\ cm^{-1}$) in aqueous solutions. The wide spectral response range and large molar absorption coefficient make it a potential photosensitizer. The electrons of crystal violet are excited to the excited state under light irradiation. The effective band alignment between crystal violet and SnS_2 promotes fast electron injection from crystal violet to the conduction band of SnS_2, thus suppressing the backfill of electrons and achieving a huge photocurrent response. In particular, the ingeniously fabricated PEC sensing platform provides an avenue for the further detection of UDG.

2.3. Construction Process Characterization of the PEC Biosensor. To demonstrate the stepwise-fabricated process of the PEC biosensor, electrochemical techniques including cyclic voltammetry (CV) and electrochemical impedance spectroscopy (EIS) were implemented in phosphate-buffered saline (PBS) (0.1 M, pH 7.4) containing 5.0 mM $[Fe(CN)_6]^{3-/4-}$ and 0.1 M KCl (see the Supporting Information for the fabrication process of the biosensor). As displayed in Figure S5a, the bare GCE shows the smallest electron-transfer resistance (R_{et}) (curve i). The R_{et} was dramatically augmented after modifying WO_3@SnS_2 (curve ii) because the poor conductivity of WO_3@SnS_2 blocks the interfacial electron communication. For 3-mercaptopropionic acid (MPA), a further increase in the R_{et} can be observed (curve iii), which could be attributed to the negative charge of MPA, preventing the electroactive probe from approaching the electrode surface. After incubation with NH_2-c-myc and monoethanolamine (MEA), the R_{et} continuously increased (curves iv and v), which can be readily attributed to the steric hindrance effect and the electrostatic repulsion effect. As expected, a larger semicircle is formed (curve vi) after incubation of the amplified products, caused by the electrostatic repulsion between the negatively charged phosphate bone and the negatively charged electroactive probe $[Fe(CN)_6]^{3-/4-}$. Furthermore, the above results have also been demonstrated by cyclic voltammetry (Figure S5b). The peak current obviously decreases with the modification of WO_3@SnS_2 (curve ii) compared with the bare GCE (curve i), which is ascribed to the hindrance of the electron transfer. After the stepwise assembling of MPA, NH_2-c-myc, MEA, and the growing G-wire nanostructure, the peak current continuously declined (curves iii, iv, v, and vi), indicating the successful construction of the PEC biosensor.

The change of the photocurrent signal was inspected to verify the construction process of the PEC sensing platform. As seen in Figure S5c, a negligible photocurrent response exists in bare GCE (curve i), and the WO_3@SnS_2 photoanode displays a notable photocurrent response (curve ii). This result indicates that the WO_3@SnS_2 possesses remarkable visible light response activity and fast electron−hole pair separation ability. The photocurrent signal decreases after fixing MPA (curve iii). When the NH_2-c-myc and MEA were modified sequentially, the photocurrent signal decreased continuously (curves iv and v), which was caused by the increase of the steric hindrance effect and the decrease of the electron-transfer efficiency. Subsequently, the G-wire nanostructure was generated, and the photocurrent signal decreased (curve vi), caused by the nonconductive properties and insulation effects of the G-wire, obstructing electron transfer between photoactive materials and electrons. Due to the sensitization effect, the resulting electrode generated an enhanced photocurrent response after bonding with crystal violet (curve vii). Generally speaking, the well-designed sensor was successfully constructed for subsequent PEC sensing of UDG activity.

2.4. Analytical Performance of the PEC Biosensor. The variation of the PEC signal of the constructed sensor depended on the amount of crystal violet, which was related to the concentration of UDG. Under optimal experimental conditions (see the Supporting Information for the optimization of the experimental conditions; Figures S6 and S7), the analytical performance of the PEC sensor for UDG detection was evaluated by measuring different concentrations of UDG according to the proposed PEC strategy. As shown in Figure 5a, with the increase of the UDG concentration, the photocurrent signal gradually increases. There is a good linear relationship between the PEC signal and the logarithm of the concentration of UDG in the range of 0.0005−1.0 U/mL (Figure 5b). The corresponding linear equation is $i = 0.444 \log C + 5.936$, with a correlation coefficient of 0.990. Also, the detection limit was calculated to be 0.00025 U/mL based on the equation of 3σ/slope, in which σ represents the standard deviation of the blank sample. Compared with reported detection methods, the developed biosensor shows a superior

https://doi.org/10.1021/acsami.1c01525
ACS Appl. Mater. Interfaces 2021, 13, 15881−15889

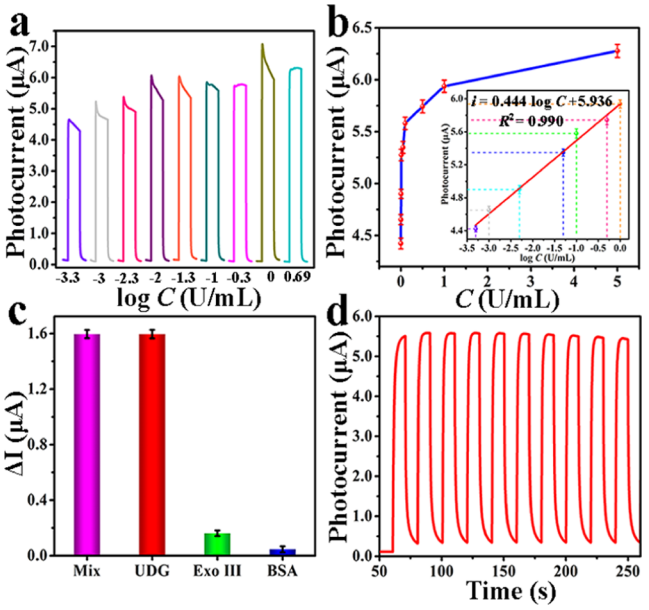

Figure 5. (a) Photocurrent response and (b) corresponding calibration curve at various concentrations of UDG. (c) Photocurrent change of the PEC biosensor corresponding to UDG (0.1 U/mL), Exo III (0.1 U/mL), and bovine serum albumin (BSA) (0.01 mg/mL), as well as the mixing system containing UDG (0.1 U/mL), Exo III (0.1 U/mL), and BSA (0.01 mg/mL). (d) Photocurrent response of the PEC biosensor to UDG (0.1 U/mL) after scanning for 10 cycles.

or comparable detection sensitivity (Table S2). It is worth noting that the pre-eminent analytical performance of the UDG assay of the PEC biosensor was attributed to the following points: (i) the 3D hierarchical nanostructures afford sufficient interfacial area and a short diffusion distance for charge carriers, and the formation of the Z-scheme heterojunction is conducive to the separation and transport of the photogenerated carriers, (ii) the UDG excision-driven enzyme-assisted dual-cycle signal amplification generates a large number of c-myc fragments, which will couple with a substantial amount of sensitizer to achieve signal amplification, and (iii) due to the band matching between crystal violet and SnS_2, the thermodynamic conditions promote the excited electron injection, effectively suppress the recombination of electrons and holes, and further enhance the photocurrent response.

2.5. Specificity, Repeatability, and Stability of the PEC Sensing Platform. To evaluate whether the fabricated PEC sensing platform has satisfactory selectivity, the exonuclease III and BSA were selected to test the system (Figure 5c). The assay was performed by substituting 0.1 U/mL UDG with 0.1 U/mL exonuclease III and 0.01 mg/mL BSA. The target UDG and the mixture system containing both UDG and the above two substances yield a significant enhancement in the photocurrent signal. Nevertheless, BSA and exonuclease III only show a negligible influence on the PEC response. This result indicates that only the target can trigger the amplification strategy, and the proposed protocol shows commendable selectivity for the UDG assay. In addition, the constructed biosensor presents good anti-interference ability for coexisting reductants (glutathione, dopamine, and ascorbic acid) in a complex biological system (Figure S8). Moreover, the repeatability of the constructed sensing platform was estimated through testing five electrodes prepared under the same conditions as UDG (0.1 U/mL). The relative standard deviation (RSD) is 2.25%. Consequently, the PEC biosensing platform possesses favorable repeatability for the UDG assay. In addition, there is an ultraweak change in photocurrent response after 10 cycles with a relative standard deviation (RSD) of 1.22% (Figure 5d), indicating that the biosensor presents excellent stability.

2.6. Practical Application Capability of the Constructed Biosensor. To confirm the application capability of the proposed PEC biosensor, the HeLa cell (a human cervical cancer cell line with higher uracil excision capacity) was chosen to implement a PEC assay (see the Supporting Information for the treatment of HeLa cells). Figure S9 displays the distinguishing photocurrent response curve of the HeLa cell lysate and the lysis buffer. A significantly stronger photocurrent response is obtained in the HeLa cell lysate than that of lysis buffer. The proposed method exhibits good performance in the HeLa cell lysate, which proves that it possesses outstanding practical application potential.

3. CONCLUSIONS

In summary, an excellent PEC biosensing platform was successfully constructed based on the Z-scheme WO_3@SnS_2 nanostructures and target excision-driven dual-cycle amplification, as well as dye sensitization, which can achieve sensitive UDG detection. The results confirm that the formation of the Z-scheme electron migration mechanism in the WO_3@SnS_2 hierarchical nanostructure expands the range of visible light capture and enhances photoelectric conversion efficiency. With the aid of the biological recognition process, signal amplification is realized on account of a distinctive G-wire structure. Moreover, the sensitizer crystal violet was fixed onto the G-wire via the $\pi-\pi$ interaction or electrostatic interaction to amplify the photocurrent response. Especially, this is the first time that crystal violet acts as a sensitizer to amplify the PEC response. In addition, dual-cycle amplification driven by UDG excision leads to generation of exponential c-myc fragments for target quantification and the formation of a G-wire structure. Also, a possible electron-transfer mechanism has been proposed by some common characterization methods and simple calculations. This work provides a new avenue for the construction of a PEC sensing platform based on dye-sensitized signal amplification.

■ ASSOCIATED CONTENT

Supporting Information

The Supporting Information is available free of charge at https://pubs.acs.org/doi/10.1021/acsami.1c01525.

Material preparation and UDG excision amplification experimental details; polyacrylamide gel electrophoresis characterization; optimization of detection conditions; and additional characterization data and DNA sequences (PDF)

■ AUTHOR INFORMATION

Corresponding Authors

Nian Bing Li − *School of Chemistry and Chemical Engineering, Southwest University, Chongqing 400715, P. R. China;* orcid.org/0000-0001-6395-2074; Email: linb@swu.edu.cn

https://doi.org/10.1021/acsami.1c01525
ACS Appl. Mater. Interfaces 2021, 13, 15881−15889

Hong Qun Luo − *School of Chemistry and Chemical Engineering, Southwest University, Chongqing 400715, P. R. China*; orcid.org/0000-0002-2254-6034; Email: luohq@swu.edu.cn

Authors

Xing Yue Zhang − *School of Chemistry and Chemical Engineering, Southwest University, Chongqing 400715, P. R. China*

Lei Han − *School of Chemistry and Chemical Engineering, Southwest University, Chongqing 400715, P. R. China*

Ling Dan Yu − *School of Chemistry and Chemical Engineering, Southwest University, Chongqing 400715, P. R. China*

Xiao Hu Wang − *School of Chemistry and Chemical Engineering, Southwest University, Chongqing 400715, P. R. China*

Yu Ling − *School of Chemistry and Chemical Engineering, Southwest University, Chongqing 400715, P. R. China*

Complete contact information is available at: https://pubs.acs.org/10.1021/acsami.1c01525

Author Contributions

X.Y.Z.: Conceptualization, methodology, investigation, data curation, formal analysis, writing—original draft, and software; L.H.: investigation and validation; L.D.Y.: data curation; X.H.W.: software; Y.L.: supervision and investigation; N.B.L.: project administration and data curation; and H.Q.L.: supervision and writing—review and editing.

Notes

The authors declare no competing financial interest.

■ ACKNOWLEDGMENTS

We acknowledge the funding provided by the National Natural Science Foundation of China (No. 21675131) and the Municipal Science Foundation of Chongqing City (No. cstc2020jcyj-zdxmX0003).

■ REFERENCES

(1) Liu, X.; Chen, M.; Hou, T.; Wang, X.; Liu, S.; Li, F. Label-free Colorimetric Assay for Base Excision Repair Enzyme Activity Based on Nicking Enzyme Assisted Signal Amplification. *Biosens. Bioelectron.* **2014**, *54*, 598−602.

(2) Stivers, J. T.; Jian, Y. L. A Mechanistic Perspective on the Chemistry of DNA Repair Glycosylases. *Chem. Rev.* **2003**, *103*, 2729−2759.

(3) Seal, G.; Brech, K.; Karp, S. J.; Cool, B. L.; Sirover, M. A. Immunological Lesions in Human Uracil DNA Glycosylase: Association with Bloom Syndrome. *Proc. Natl. Acad. Sci. U.S.A.* **1988**, *85*, 2339−2343.

(4) Imai, K.; Slupphaug, G.; Lee, W. I.; Revy, P.; Nonoyama, S.; Catalan, N.; Yel, L.; Forveille, M.; Kavli, B.; Krokan, H. E.; Ochs, H. D.; Fischer, A.; Durandy, A. Human Uracil-DNA Glycosylase Deficiency Associated with Profoundly Impaired Immunoglobulin Class-Switch Recombination. *Nat. Immunol.* **2003**, *4*, 1023−1028.

(5) Hoeijmakers, J. H. J. Genome Maintenance Mechanisms for Preventing Cancer. *Nature* **2001**, *411*, 366−374.

(6) Zhao, W. W.; Xu, J. J.; Chen, H. Y. Photoelectrochemical Bioanalysis: The State of The Art. *Chem. Soc. Rev.* **2015**, *44*, 729−741.

(7) Shu, J.; Tang, D. P. Recent Advances in Photoelectrochemical Sensing: From Engineered Photoactive Materials to Sensing Devices and Detection Modes. *Anal. Chem.* **2020**, *92*, 363−377.

(8) Wang, H.; Zhang, B. H.; Zhao, F. Q.; Zeng, B. Z. One-Pot Synthesis of N-Graphene Quantum Dot-Functionalized I-BiOCl Z-Scheme Cathodic Materials for "Signal-Off" Photoelectrochemical Sensing of Chlorpyrifos. *ACS Appl. Mater. Interfaces* **2018**, *10*, 35281−35288.

(9) Zeng, R. J.; Luo, Z. B.; Su, L. S.; Zhang, L. J.; Tang, D. P.; Niessner, R.; Knopp, D. Palindromic Molecular Beacon Based Z-Scheme BiOCl-Au-CdS Photoelectrochemical Biodetection. *Anal. Chem.* **2019**, *91*, 2447−2454.

(10) Zhang, L.; Luo, Z.; Zeng, R.; Zhou, Q.; Tang, D. All-Solid-State Metal-Mediated Z-Scheme Photoelectrochemical Immunoassay with Enhanced Photoexcited Charge-Separation for Monitoring of Prostate-Specific Antigen. *Biosens. Bioelectron.* **2019**, *134*, 1−7.

(11) Lv, S. Z.; Zhang, K. Y.; Zeng, Y. Y.; Tang, D. P. Double Photosystems-Based 'Z-Scheme' Photoelectrochemical Sensing Mode for Ultrasensitive Detection of Disease Biomarker Accompanying Three-Dimensional DNA Walker. *Anal. Chem.* **2018**, *90*, 7086−7093.

(12) Tu, W. G.; Zhou, Y.; Feng, S. C.; Xu, Q. F.; Li, P.; Wang, X. Y.; Xiao, M.; Zou, Z. G. Hollow Spheres Consisting of $Ti_{0.91}O_2$/CdS Nanohybrids for CO_2 Photofixation. *Chem. Commun.* **2015**, *51*, 13354−13357.

(13) Liu, C.; Tang, J. Y.; Chen, H. M.; Liu, B.; Yang, P. D. A Fully Integrated Nanosystem of Semiconductor Nanowires for Direct Solar Water Splitting. *Nano Lett.* **2013**, *13*, 2989−2992.

(14) Wang, Y.; Zhang, Z. Z.; Zhang, L.; Luo, Z. B.; Shen, J. N.; Lin, H. X.; Long, J. L.; Wu, J. C. S.; Fu, X. Z.; Wang, X. X.; Li, C. Visible-Light Driven Overall Conversion of CO_2 and H_2O to CH_4 and O_2 on 3D-SiC@2D-MoS_2 Heterostructure. *J. Am. Chem. Soc.* **2018**, *140*, 14595−14598.

(15) Yu, W.; Chen, J.; Shang, T.; Chen, L.; Gu, L.; Peng, T. Direct Z-Scheme g-C_3N_4/WO_3 Photocatalyst with Atomically Defined Junction for H_2 Production. *Appl. Catal., B* **2017**, *219*, 693−704.

(16) Yu, W. L.; Zhang, S.; Chen, J. X.; Xia, P. F.; Richter, M. H.; Chen, L. F.; Xu, W.; Jin, J. P.; Chen, S. P.; Peng, T. Y. Biomimetic Z-Scheme Photocatalyst with a Tandem Solid-State Electron Flow Catalyzing H_2 Evolution. *J. Mater. Chem. A* **2018**, *6*, 15668−15674.

(17) Huang, Y.; Guo, Z.; Liu, H.; Zhang, S.; Wang, P.; Lu, J.; Tong, Y. Heterojunction Architecture of N-Doped WO_3 Nanobundles with Ce_2S_3 Nanodots Hybridized on a Carbon Textile Enables a Highly Efficient Flexible Photocatalyst. *Adv. Funct. Mater.* **2019**, *29*, No. 1903490.

(18) Zeng, Y.; Guo, N.; Li, H. Y.; Wang, Q. Y.; Xu, X. J.; Yu, Y.; Han, X. R.; Yu, H. W. A Novel Route to Manufacture WO_3@MoS_2 p-n Heterostructure Hollow Tubes with Enhanced Photocatalytic activity. *Chem. Commun.* **2019**, *55*, 683−686.

(19) Wang, X. D.; Huang, Y. H.; Liao, J. F.; Jiang, Y.; Zhou, L.; Zhang, X. Y.; Chen, H. Y.; Kuang, D. B. In Situ Construction of a Cs_2SnI_6 Perovskite Nanocrystal/SnS_2 Nanosheet Heterojunction with Boosted Interfacial Charge Transfer. *J. Am. Chem. Soc.* **2019**, *141*, 13434−13441.

(20) Zhang, F. F.; Chen, Y. J.; Zhou, W.; Ren, C.; Gao, H. J.; Tian, G. H. Hierarchical SnS_2/$CuInS_2$ Nanosheet Heterostructure Films Decorated with C_{60} for Remarkable Photoelectrochemical Water Splitting. *ACS Appl. Mater. Interfaces* **2019**, *11*, 9093−9101.

(21) Zhang, X. Y.; Liu, S. G.; Zhang, W. J.; Wang, X. H.; Han, L.; Ling, Y.; Li, N. B.; Luo, H. Q. Photoelectrochemical Platform for Glucose Sensing Based on g-C_3N_4/$ZnIn_2S_4$ Composites Coupled with Bi-Enzyme Cascade Catalytic in-situ Precipitation. *Sens. Actuators, B* **2019**, *297*, No. 126818.

(22) Wang, L. P.; Meng, Y.; Zhang, C. X.; Xiao, H. B.; Li, Y. L.; Tan, Y. M.; Xie, Q. J. Improving Photovoltaic and Enzymatic Sensing Performance by Coupling a Core-Shell Au Nanorod@TiO_2 Heterostructure with the Bioinspired L-DOPA Polymer. *ACS Appl. Mater. Interfaces* **2019**, *11*, 9394−9404.

(23) Song, Z.; Fan, G. C.; Li, Z. M.; Gao, F. X.; Luo, X. L. Universal Design of Selectivity-Enhanced Photoelectrochemical Enzyme Sensor: Integrating Photoanode with Biocathode. *Anal. Chem.* **2018**, *90*, 10681−10687.

(24) Ye, C.; Wang, M. Q.; Gao, Z. F.; Zhang, Y.; Lei, J. L.; Luo, H. Q.; Li, N. B. Ligating Dopamine as Signal Trigger onto the Substrate via Metal-Catalyst-Free Click Chemistry for "Signal-On" Photo-

electrochemical Sensing of Ultralow MicroRNA Levels. *Anal. Chem.* **2016**, *88*, 11444−11449.
(25) Zeng, R.; Zhang, L.; Luo, Z.; Tang, D. Palindromic Fragment-Mediated Single-Chain Amplification: An Innovative Mode for Photoelectrochemical Bioassay. *Anal. Chem.* **2019**, *91*, 7835−7841.
(26) Lin, Y. X.; Zhou, Q.; Tang, D. P. Dopamine-Loaded Liposomes for in-Situ Amplified Photoelectrochemical Immunoassay of AFB_1 to Enhance Photocurrent of Mn^{2+}-Doped $Zn_3(OH)_2V_2O_7$ Nanobelts. *Anal. Chem.* **2017**, *89*, 11803−11810.
(27) Ye, C.; Wang, M. Q.; Luo, H. Q.; Li, N. B. Label-Free Photoelectrochemical "Off-On" Platform Coupled with G-Wire-Enhanced Strategy for Highly Sensitive MicroRNA Sensing in Cancer Cells. *Anal. Chem.* **2017**, *89*, 11697−11702.
(28) Yan, Z. Y.; Wang, Z. H.; Miao, Z.; Liu, Y. Dye-Sensitized and Localized Surface Plasmon Resonance Enhanced Visible-Light Photoelectrochemical Biosensors for Highly Sensitive Analysis of Protein Kinase Activity. *Anal. Chem.* **2016**, *88*, 922−929.
(29) Zeng, X. X.; Tu, W. W.; Li, J.; Bao, J. C.; Dai, Z. H. Photoelectrochemical Biosensor Using Enzyme-Catalyzed in Situ Propagation of CdS Quantum Dots on Graphene Oxide. *ACS Appl. Mater. Interfaces* **2014**, *6*, 16197−16203.
(30) Hou, T.; Zhang, L. F.; Sun, X. Z.; Li, F. Biphasic Photoelectrochemical Sensing Strategy Based on in situ Formation of CdS Quantum Dots for Highly Sensitive Detection of Acetylcholinesterase Activity and Inhibition. *Biosens. Bioelectron.* **2016**, *75*, 359−364.
(31) Kong, D. M.; Ma, Y. E.; Guo, J. H.; Yang, W.; Shen, H. X. Fluorescent Sensor for Monitoring Structural Changes of G-Quadruplexes and Detection of Potassium Ion. *Anal. Chem.* **2009**, *81*, 2678−2684.
(32) Wang, S.; Zhao, J. H.; Lu, S. S.; Sun, J.; Yang, X. R. A Duplex Connection Can Further Illuminate G-Quadruplex/Crystal Violet Complex. *Chem. Commun.* **2019**, *55*, 1911−1914.
(33) Wang, S.; Lu, S. S.; Zhao, J. H.; Yang, X. R. A Ratiometric Fluorescent DNA Radar Based on Contrary Response of DNA/Silver Nanoclusters and G-Quadruplex/Crystal Violet. *ACS Appl. Mater. Interfaces* **2019**, *11*, 25066−25073.
(34) Kong, D. M.; Ma, Y. E.; Wu, J.; Shen, H. X. Discrimination of G-Quadruplexes from Duplex and Single-Stranded DNAs with Fluorescence and Energy-Transfer Fluorescence Spectra of Crystal Violet. *Chem. - Eur. J.* **2009**, *15*, 901−909.
(35) Ren, W.; Zhang, Y.; Chen, H. G.; Gao, Z. F.; Li, N. B.; Luo, H. Q. Ultrasensitive Label-Free Resonance Rayleigh Scattering Aptasensor for Hg^{2+} Using Hg^{2+}-Triggered Exonuclease III-Assisted Target Recycling and Growth of G-Wires for Signal Amplification. *Anal. Chem.* **2016**, *88*, 1385−1390.
(36) Cui, Y. X.; Feng, X. N.; Wang, Y. X.; Pan, H. Y.; Pan, H.; Kong, D. M. An Integrated-Molecular-Beacon Based Multiple Exponential Strand Displacement Amplification Strategy for Ultrasensitive Detection of DNA Methyltransferase Activity. *Chem. Sci.* **2019**, *10*, 2290−2297.
(37) Zhou, M. X.; Teng, X. C.; Li, Y.; Deng, R. J.; Li, J. H. Cascade Transcription Amplification of RNA Aptamer for Ultrasensitive MicroRNA Detection. *Anal. Chem.* **2019**, *91*, 5295−5302.
(38) Yang, Y.-Y.; Zhang, X.-G.; Niu, C.-G.; Feng, H.-P.; Qin, P.-Z.; Guo, H.; Liang, C.; Zhang, L.; Liu, H.-Y.; Li, L. Dual-channel Charges Transfer Strategy with Synergistic Effect of Z-scheme Heterojunction and LSPR Effect for Enhanced Quasi-Full-Spectrum Photocatalytic Bacterial Inactivation: New Insight into Interfacial Charge Transfer and Molecular Oxygen Activation. *Appl. Catal., B* **2020**, *264*, No. 118465.
(39) Shown, I.; Samireddi, S.; Chang, Y.-C.; Putikam, R.; Chang, P.-H.; Sabbah, A.; Fu, F.-Y.; Chen, W.-F.; Wu, C.-I.; Yu, T.-Y.; Chung, P.-W.; Lin, M. C.; Chen, L.-C.; Chen, K.-H. Carbon-doped SnS_2 Nanostructure as a High-Efficiency Solar Fuel Catalyst under Visible Light. *Nat. Commun.* **2018**, *9*, No. 169.
(40) Ye, C.; Wang, M. Q.; Li, L. J.; Luo, H. Q.; Li, N. B. Fabrication of $Pt/Cu_3(PO_4)_2$ Ultrathin Nanosheet Heterostructure for Photoelectrochemical MicroRNA Sensing Using Novel G-Wire-Enhanced Strategy. *Nanoscale* **2017**, *9*, 7526−7532.
(41) Jiang, Z.; Wan, W.; Li, H.; Yuan, S.; Zhao, H.; Wong, P. K. A Hierarchical Z-Scheme α-Fe_2O_3/g-C_3N_4 Hybrid for Enhanced Photocatalytic CO_2 Reduction. *Adv. Mater.* **2018**, *30*, No. 1706108.
(42) Yang, J.; Hao, J. Y.; Xu, S. Y.; Wang, Q.; Dai, J.; Zhang, A. C.; Pang, X. C. $InVO_4/\beta$-$AgVO_3$ Nanocomposite as a Direct Z-Scheme Photocatalyst toward Efficient and Selective Visible-Light-Driven CO_2 Reduction. *ACS Appl. Mater. Interfaces* **2019**, *11*, 32025−32037.
(43) Yu, W. L.; Xu, D. F.; Peng, T. Y. Enhanced Photocatalytic Activity of g-C_3N_4 for Selective CO_2 Reduction to CH_3OH via Facile Coupling of ZnO: A Direct Z-scheme Mechanism. *J. Mater. Chem. A* **2015**, *3*, 19936−19947.

https://doi.org/10.1021/acsami.1c01525
ACS Appl. Mater. Interfaces 2021, 13, 15881−15889